Mechanical Properties of Si Nanowires as Revealed by in Situ Transmission Electron Microscopy and Molecular Dynamics Simulations

Dai-Ming Tang,[†,||] Cui-Lan Ren,[‡,||] Ming-Sheng Wang,[†,§] Xianlong Wei,[†] Naoyuki Kawamoto,[†] Chang Liu,*[,‡] Yoshio Bando,[†] Masanori Mitome,[†] Naoki Fukata,[†] and Dmitri Golberg*[,†]

[†]International Center for Materials Nanoarchitectonics (MANA), National Institute for Materials Science (NIMS), Namiki 1-1, Tsukuba, Ibaraki 305-0044 Japan

[‡]Shenyang National Laboratory for Materials Science, Institute of Metal Research, Chinese Academy of Sciences, 72 Wenhua Road, Shenyang 110016 China

S Supporting Information

ABSTRACT: Deformation and fracture mechanisms of ultrathin Si nanowires (NWs), with diameters of down to ∼9 nm, under uniaxial tension and bending were investigated by using in situ transmission electron microscopy and molecular dynamics simulations. It was revealed that the mechanical behavior of Si NWs had been closely related to the wire diameter, loading conditions, and stress states. Under tension, Si NWs deformed elastically until abrupt brittle fracture. The tensile strength showed a clear size dependence, and the greatest strength was up to 11.3 GPa. In contrast, under bending, the Si NWs demonstrated considerable plasticity. Under a bending strain of <14%, they could repeatedly be bent without cracking along with a crystalline-to-amorphous phase transition. Under a larger strain of >20%, the cracks nucleated on the tensed side and propagated from the wire surface, whereas on the compressed side a plastic deformation took place because of dislocation activities and an amorphous transition.

KEYWORDS: Silicon nanowires, nanomechanics, in situ electron microscopy, tensile, bending, size effects
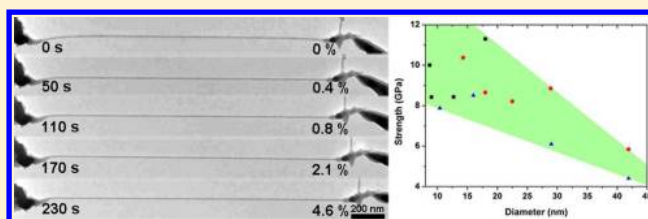
Si NWs have attracted widespread research interest because of their special properties and broad applications in electrical and optical nanodevices and nanoelectromechanical systems (NEMS).[1−7] To design and fabricate reliable Si-based nanodevices, a clear understanding of the mechanical properties and behaviors of nanoscale Si building blocks is vitally important. Because of a size effect, the mechanical behaviors of nanoscale materials can be quite different from those of their bulk counterparts.[8−17] Therefore, many studies have been conducted to elucidate the deformation and fracture mechanisms of Si NWs using various methods, such as bending in an atomic force microscope (AFM), tensile tests in a scanning electron microscope (SEM) and a transmission electron microscope (TEM), and also theoretical simulations.[18−32] However, controversial results have been reported with respect to the basic question, are Si NWs brittle or ductile at room temperature? For example, it was reported that Si NWs were brittle and possessed a sole elastic deformation before catastrophic fracture.[20,24,27,28,31,33] In contrast, Kizuka et al. and Han et al. demonstrated that Si NWs could tolerate substantial plastic deformation under both uniaxial tension and bending.[18,22,26,32] In addition, a brittle-to-ductile transition from 310 to 400 nm was reported by Östlund et al. for the nanoscale Si pillars under compression.[25] By using molecular dynamics (MD) simulations, Kang et al. found that Si NWs could fracture

in either brittle or ductile manners under tension, depending on their diameter and growth direction.[21,30] One reason for the regarded controversy is that in each work the mechanical properties of Si NWs were evaluated using a single method and under one loading mode, whereas it is well known that in addition to intrinsic parameters, such as chemical bonding, the wire diameter, and crystalline defects, external factors such as loading conditions and stress states could also have important influences.[34]

In this work, we adopted in-tandem in situ TEM and MD simulations to investigate the mechanical properties and behaviors of ultrathin Si NWs (diameter down to ∼9 nm) under both uniaxial tension and bending loading conditions. Compared to other techniques, in situ TEM enables the direct, real-time observation of structural alternations under measurements with high resolution. Also, MD simulations can provide detailed atomic deformation mechanisms. Using the combination of these two techniques, we found that the NW diameter, loading conditions, and stress states all have important influences on the deformation and fracture mechanisms, and there is no simple answer to the above-mentioned question of

whether Si NWs are brittle or ductile. The answer is more complex, and the Si NW mechanics is much richer as thoroughly discussed below.

The Si NWs employed in this study were grown on a Si substrate at 550 °C in flowing silane gas (100% SiH_4 at 19 sccm) as a Si reactant and nitrogen (N_2 at 30 sccm) as a carrier gas in a chemical vapor deposition (CVD) system.[35] The background pressure in the CVD chamber was set at 2×10^{-6} Pa in order to eliminate possible contaminants, in particular, those from residual oxygen that may easily oxidize Si NW surfaces during growth.[36] Nanocolloidal gold particles of 3 nm diameter were used as metal catalysts during the vapor−liquid−solid (VLS) growth.

The Si nanowires were characterized by TEM, and the results are demonstrated in Figures 1 and S1. A low-magnification TEM image (Figure 1a) shows that the nanowires are straight and possess uniform diameters. A selected area electron diffraction (SAED) pattern is shown in Figure 1b. The sharp diffraction spots reveal the high quality of the nanowires. The SAED pattern can be indexed as the [110] zone axis pattern, and the wire growth direction is along [−111]. The corresponding HRTEM image shows clear lattice fringes of Si (−111), consistent with the SAED pattern. TEM and HRTEM images of another nanowire are shown in Figure S1. It is worth mentioning that there is only a very thin amorphous SiO_2 layer (1 to 2 nm) on the wire surface; therefore, it becomes possible to evaluate the intrinsic properties of Si NWs. Also, the surface is not flat on the nanometer scale, as shown by an arrow in Figure S1b, indicating the existence of surface defects. The chemical purity of the nanowires was further confirmed by electron energy loss spectroscopy (EELS, Figure S1c) and energy-dispersive X-ray spectroscopy (EDS, Figure S1d). In accord with the HRTEM results, the clear Si-L_{23} edge was identified in the EELS, whereas no impurity signals, such as from carbon and/or oxygen, were detected. EDS spectra of a single Si NW on a carbon film and hole of the TEM grid are presented (Figure S1d). For both spectra, strong silicon signals from the Si NW and copper signals from the TEM grid were detected. For the sample stretched over the TEM grid hole, negligible amounts of carbon and oxygen could be identified, whereas for the Si NW on the carbon film, a small amount of oxygen was evident along with strong carbon signals.

Direct tensile tests on the Si NWs were conducted by using a TEM−AFM platform (Nanofactory Instruments AB).[37−44] The experimental configuration is shown in Figure 2a. Details of the experimental procedure, including the calibration of the AFM
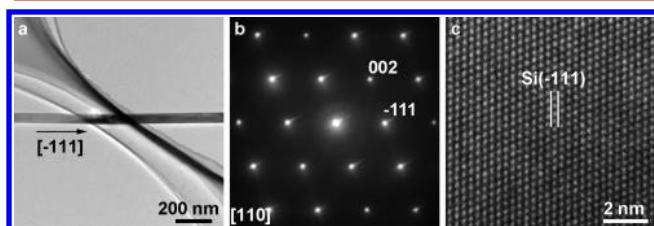

Figure 1. (a) TEM image of a single Si NW on the holey TEM grid. (b) Corresponding selected-area electron diffraction (SAED) pattern, which can be indexed as the [110] zone axis pattern, and the wire growth direction is along [−111]. (c) HRTEM image of the Si NW revealing the high crystallinity and clearly resolved lattice fringes of Si(−111).
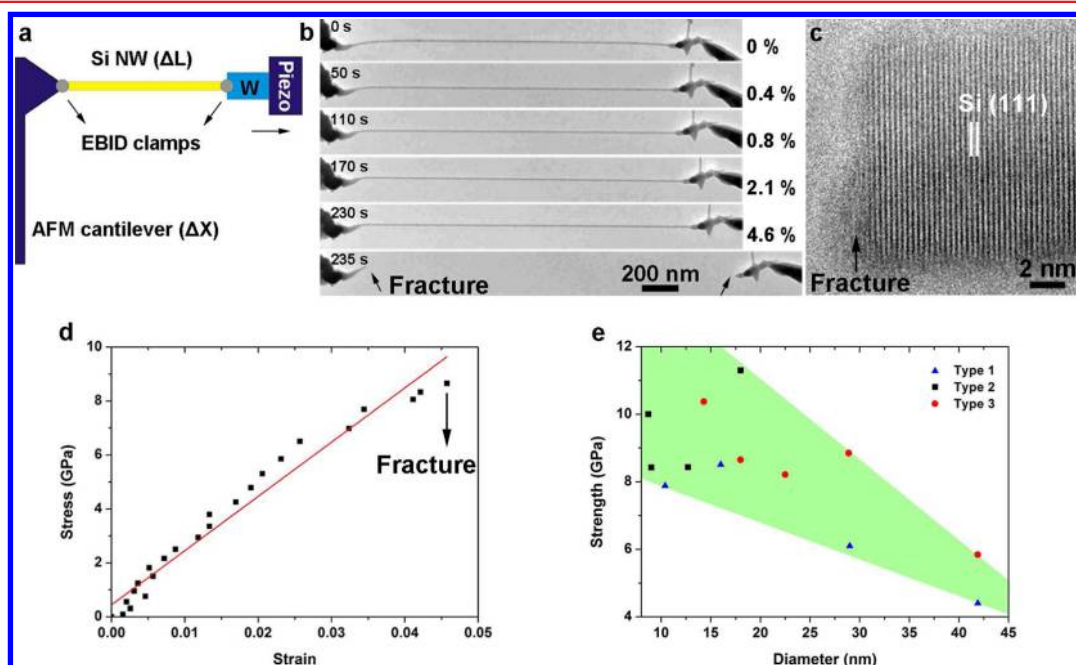

Figure 2. In situ TEM tensile tests on a single Si NW. (a) Schematic illustration of the experimental configuration. A Si NW was clamped by electron-beam-induced carbon deposition between the AFM cantilever and the tungsten tip. An elongation of the nanowire (ΔL) and a displacement of the cantilever (Δx) were recorded in situ for the calculations of strains and stresses, respectively. (b) Snapshots of the tensile elongation and fracture process. Uniform elongation was observed until the abrupt fracture at two positions simultaneously. (c) HRTEM image of the Si NW fracture surface. (d) Typical strain−stress curve illustrating a linear elastic deformation until abrupt failure with the values of fracture stress and strain of 8.7 GPa and 4.6%, respectively. (e) Band of the measured ultimate tensile strength values as a function of the Si NW diameters, revealing a clear trend of increasing strength with decreasing diameter. Fractures with rupture sites close to the clamp (type 1), in the middle (type 2) and at two positions simultaneously (type 3), are plotted with blue, black, and red symbols, respectively.

cantilever spring constants, and aligning processes can be found in the Supporting Information. These processes are crucial for accurate assessments of the mechanical properties under uniaxial conditions.[13−17] One end of a Si NW was clamped to the AFM cantilever, and the other end was tightly adhered to the W tip via an electron-beam-induced deposition (EBID) technique.[42,43,45−47] Then the nanowire was stretched, under retraction of the W tip, until the wire was ruptured (Supporting Information, Movies S1−S3). During tension, an elongation of the nanowire (ΔL) and a cantilever displacement (Δx) were recorded for accurate calculations of the strains and stresses. A typical tensile elongation process of a Si NW with an 18 nm diameter is demonstrated in Figure 2b. The nanowire was elongated uniformly at an average strain rate of $\sim 10^{-4}$/s until it was abruptly fractured at a 4.6% strain. Different types of fractures have been observed (Figure S2). Some Si NWs (type 1) fractured close to the clamps, likely because of stress concentration at defects induced during the clamp deposition processes. Some Si NWs (type 2) were broken in the middle, possibly because of prime crack nucleation and propagation. Other Si NWs (type 3) fractured in an abrupt manner at the two positions simultaneously, indicating that the nanowire had reached its elastic limit, as shown in Figures 2b and S2c. Regardless of the fracture site positions, the fractures were all brittle by cleavage along the (111) planes, without noticeable plastic deformation. A HRTEM image of a typical fracture surface is demonstrated in Figure 2c; it is flat and perpendicular to the axial direction. No necking or sliding was observed. A typical strain−stress curve is shown in Figure 2d. A linear elastic deformation was recorded before an abrupt decrease in the stress caused by the nanowire failure. By measuring the displacement of the AFM cantilever, we obtained the applied force and calculated the maximum force to be ~ 1890 nN. Correspondingly, the fracture strength was calculated using $\sigma = (k\Delta x/\cos\theta)/S$, where $k = 6.9$ N/m is the spring constant of the AFM cantilever, Δx is the measured displacement of the AFM cantilever, θ is the angle between the Si NW and the deflection of the AFM cantilever, and $S = \pi d^2/4$ is the cross-sectional area of the fractured end, where d is the nanowire diameter. The strain was obtained by measuring the elongation of the Si NW using video snapshots. The measured Young's modulus was ~ 201 GPa, which is close to that of bulk Si in the [111] direction (187 GPa).[48] The ultimate tensile strength was calculated to be ~ 8.7 GPa. Overall, more than 10 individual nanowires were successfully tested, and a summarizing plot of the measured tensile strength against the nanowire diameters is demonstrated in Figure 2e. Notable scattering of the strength values is apparent, especially for the narrower NWs. Besides that scattering, the strength figures show a clear dependence on the wire diameter. When the diameter decreased from ~ 42 to ~ 9 nm, the strength increased from 4.4 to 11.3 GPa. It was also found that the strength was related to the fracture mode. The nanowires with type 1 fractures constituted the lower band, whereas the nanowires with type 2 and 3 fractures exhibited higher strength.

Because there was only a very thin oxide layer on the Si NWs, it was possible to measure the pristine nanowire's intrinsic properties. In addition, during the tensile tests, no current was passed through the wires and the temperature was kept at room temperature. Furthermore, the electron beam current was kept low (1 to 2 A cm^{-2}) and the measurements were carried out at low magnification to reduce or, likely, to eliminate the effects of electron irradiation. Several important

features were found during our tensile tests. First, the fracture surface was flat and along the (111) plane. Second, the measured tensile strength values were distributed over a rather wide range. Third, the tensile strength was closely dependent on the nanowire diameter. All of these features could be understood in the framework of Griffith theory describing brittle fractures.[49] The fracture strength is dependent on the size of a crack, following the equation $\sigma = (2E\gamma/\pi a)^{1/2}$, where σ, E, γ, and a are the fracture strength, Young's modulus, specific surface energy, and crack half-length, respectively. Because of the lowest specific surface energy, the (111) plane is the ideal cleavage plane for Si.[50] Because the defects or crack sizes are usually statistically distributed, the corresponding fracture strength values may also be scattered over some range. The NWs fractured close to the clamp positions might have induced defects as stress concentrators produced during the EBID process, and therefore the tensile strength was lowered (Figure S2a). The fractures at high stresses of up to 11.3 GPa might originate from surface defects such as surface steps (Figure 1b), which affected the intrinsic tensile strength of Si NWs. Because of the smaller surface areas of the thinner NWs, the probability of such surface defects is accordingly smaller, which resulted in the higher tensile strength values. To verify the fracture mechanism, multiple tensile tests were conducted on a single Si NW (Figure S3). After the NW was fractured, it was then reconnected by the EBID method for the second and third tests. It was observed that the first two fracture sites were close to the left and right clamps, whereas the third one was in the middle of the structure. Accordingly, the measured fracture forces increased from 838 to 1596 to 2741 nN, consistent with Griffith theory. Because the fracture site was determined by the weakest spot with the largest defect and/or crack, when the nanowire was reconnected, the smaller defect or crack required a higher tensile stress at the fracture.

MD simulations were carried out to gain deeper insight into the atomic fracture mechanisms of the Si NWs (Movie S4). The simulation started from the defect free [111]-oriented Si NW, as based on our HRTEM observations. After the structural relaxation, however, the surface was reconstructed and deviated from the perfect crystalline structure, as revealed by the nonuniform local potential at the surface (Figure 3a). According to the simulation, the fracture starts from the
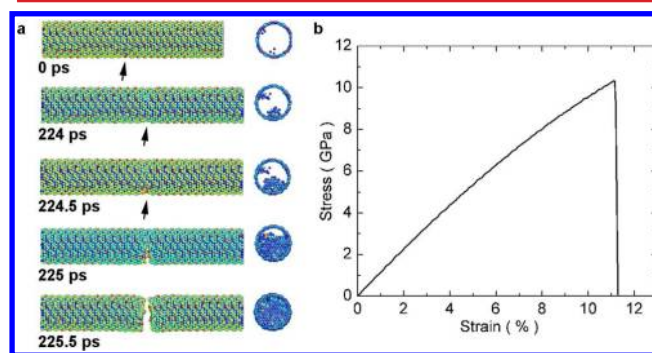

Figure 3. MD-simulated tensile test of a Si NW, 5 nm in diameter. (a) Simulated tension and rupture process. The arrows followed the evolution from the surface defect to the initialization of a massive crack. The insets are the axial views of the nucleation and propagation of the crack. The atoms are colored by their local energy, and only the atoms with higher potential energy are visible. (b) Simulated strain−stress curve of the Si NW. The nanowire deforms elastically until abrupt fracture occurs.

surface (Figure 3a), probably from the surface defects with a size of several atoms, as indicated by the arrows. Once the crack was initiated, it propagated very fast through the whole nanowire, within 1.5 ps in the simulations. As a result of the fast nucleation and propagation of the crack, the nanowire fractured abruptly, leaving a flat fracture surface that is perpendicular to the tension direction. Figure 3b is the corresponding strain−stress plot of the tensile test. A linear elastic relationship was observed until the nanowire fractured, in good agreement with the in situ observations.

Bending tests were carried out to get a comprehensive assessment of the mechanical behavior of Si NWs (Movies S5−S6). In contrast to the brittle behavior under uniaxial tension, the Si NWs showed considerable plastic deformation under bending. The bending strain was calculated according to the equation $\varepsilon_{bending} = r/(r + R)\%$, where r and R are the radius of the Si NW and the radius of curvature of the bent nanowire, respectively.[26,32,51,52] When the maximum bending strain was kept lower than 14.1% (Figure S4), surprisingly the Si NW with a diameter of 8.6 nm could be bent repeatedly over several cycles without cracking or fracture, along with a crystalline-to-amorphous transition. Figure 4 demonstrates the bending test to larger strains of a Si NW with a diameter of 25.3 nm. Clear contrasts due to strain or defect formation were observed at a lower strain (Figure 4b). A crack was found on the tensed side when the bending strain reached about 20%. Under further
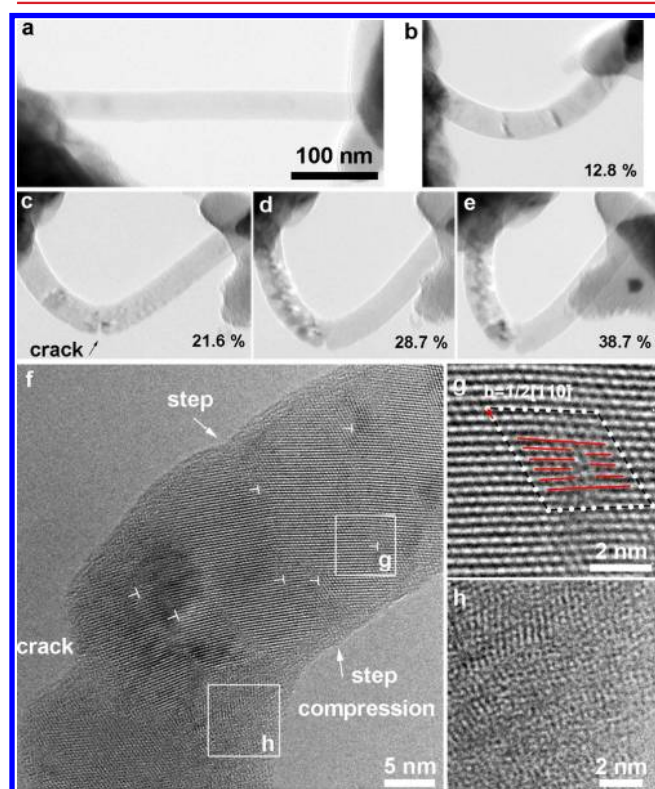
bending, the crack became wider; however, even at a bending strain of 38.7%, the nanowire did not fail completely. The crack did not propagate through the whole nanowire but became blunt at about the middle of the cross-section, probably because of a plastic deformation at the crack tip. To understand the deformation mechanism, careful HRTEM observations were carried out on the nanowire in Figure 4d, and the results are presented in Figure 4f−h. In contrast to the crack on the tensed side, dislocations were found around the severe deformation area along with the surface steps. A magnified TEM image of a dislocation is demonstrated in Figure 4g. The Burgers vector of the dislocation was determined to be $\frac{1}{2}[110]$ by drawing a Burgers circuit around the core area, as indicated by the white dots and red arrow. In addition, red lines were marked as a guide to the eye while pointing out the dislocation. It was noted that the bending strain was not uniformly distributed after the initiation of the crack on the tensed side and the area with severe bending strain had been transformed into amorphous structures, as revealed by HRTEM in Figure 4h. The existence of a high density of dislocations and amorphization in the severely strained area indicates that the structural mechanism behind the plasticity is the dislocations nucleation, their interactions, and the final crystalline−amorphous transition, which are processes that have been thoroughly studied by Han's group.[26,32]

The bending process of Si NWs was also simulated by the MD method (Movie S7). Colors were assigned according to their local shear strain for a better display of the plastic deformation. According to the simulations (Figure 5), in the beginning the Si NW was bent uniformly. At low bending strain, shear displacements occurred on the compressed side, as
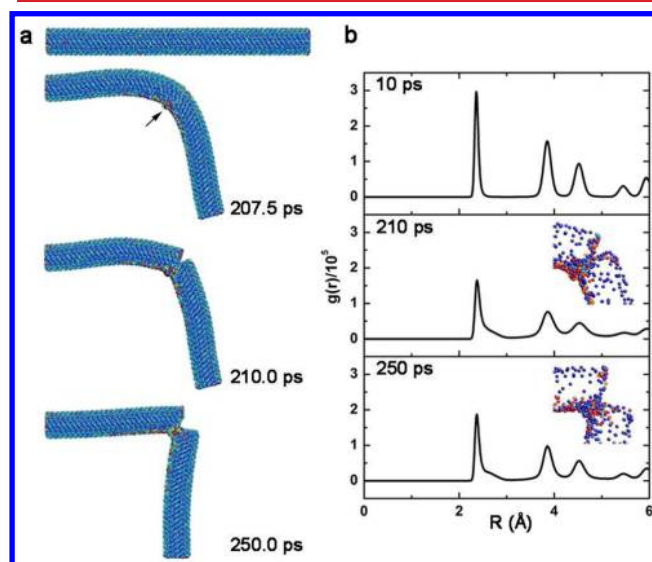

Figure 4. In situ TEM bending test on a single Si NW with a diameter of 25.3 nm. (a−e) TEM images of the bending process. (b) Strain contrast was observed at a low strain. (c) The crack was initialized at a strain of 21.6%. (d, e) Under a higher bending strain, the crack propagated. (f) HRTEM image of the Si NW in d. On the tensed side, a crack was identified. On the compressed side, the structure became amorphous. Dislocations were observed around the severe deformation zone, and steps were found on the surface. (g, h) HRTEM images of dislocation and the amorphized area.

Figure 5. MD-simulated bending test on a single Si NW, 5 nm in diameter. (a) Simulated bending process. Atomic steps were observed on the compression side at 207.5 ps. Then a crack was initialized on the tensed side at a bending strain of ~21.5%. Atom colors were assigned by their local shear strain. (b) Radial distribution functions (RDF) of the Si NW at different stages, with detailed atomic structures by shear displacement mode. (Only the atoms with a local shear strain larger than 0.5 are visible). The starting model wire was well crystallized, as featured by the sharp RDF peaks. During and after bending, the RDF peaks became wider and lower, indicating the formation of a disordered structure, which was confirmed by the detailed atomic structure at the crack tip.

Table 1. Comparison of the Results of Han et al., Gordon et al., and Our Work

	diameter (nm)	loading	orientation	defects	strain rate	conclusions
Han et al.[22]	15–70	tension	[110]	defect-free[32]	$\sim 10^{-5}$/s	ductile
Gordon et al.[24]	100–700	bending	[111]	twins and facets	10–30 nm/s	brittle
our work	9–42	tension, bending	[111]	surface steps	$\sim 10^{-4}$/s	brittle/tension, ductile/bending

indicated by the red atoms. An atomic step was identified on the compressed side, indicating slipping via dislocation activities. On the tensed side, no shear displacements were observed, indicating an elastic deformation. At a bending strain of about 21.5%, a crack was initialized on the tensed side, which is consistent with our in situ TEM observations. It propagated quickly, and the bending strain was then highly localized around the crack tip. On the compressed side, enormous plastic deformation was observed. The shear displacement distribution and the radial distribution functions both confirmed the formation of amorphous structures (Figure 5b).

Our observations of the distinctly different deformation and fracture behaviors on the tensed and compressed nanowire sides imply the prime importance of the loading conditions and stress states for the overall mechanical behavior of Si NWs. Mechanical analyses were carried out to understand the dramatically different mechanical behaviors of the Si NWs under uniaxial tension and bending. Fractures could be categorized into two basic types: (i) brittle by cracking and (ii) ductile by plastic deformation, usually in the form of dislocation activities. The nucleation of cracks is related to the axial tensile stresses, and the activation of dislocations is related to the shear stresses. Under different loading conditions, the stress states are different and therefore may result in different mechanical behaviors. A stress state parameter (α) of the ratio between the maximum shear stress and the maximum axial tensile stress could be defined to describe the influence of the stress state on the ductility of a material: $\alpha = (\tau_{max})/(S_{max}) = (\sigma_1 - \sigma_3)/(2[\sigma_1 - \nu(\sigma_2 + \sigma_3)])$, where τ_{max}, S_{max}, $\sigma_{1,2,3}$, and ν are the maximum shear stress, maximum tensile stress, three principal stresses, and Poisson ratio, respectively.[34] The smaller the stress state parameter, the "harder" the stress state, leading to a material that tends to be more brittle. The stress-state parameters for uniaxial tension and compression states are 0.5 and ~2 (assuming a Poisson ratio of 0.25), respectively. As a result, materials are usually more brittle under tension than under compression. The stress states under bending are more complex. The axial stresses are largest on the surfaces, with one side being under tension and the other side being under compression. Therefore, although the Si NWs were brittle under tension, it is not surprising that under bending and compression loading conditions they could have pronounced plasticity by the activation of dislocations followed by an amorphous transition on the compressed side.

The mechanical properties and behaviors of Si NWs have been intensively investigated; however, different or even contradictory results have been reported for both under tension and bending loading conditions. For example, tensile tests have been conducted in SEM.[27,28,31] A brittle fracture was reported for the Si NWs, despite a wide range of diameters studied, from 15 to 60 nm in Zhu's work[27] to 200–300 nm in Zhang's report[28] to 268–840 nm in Steighner's paper.[31] However, ductile fractures were reported using in situ TEM tension by Kizuka et al.[18] and Han et al.[22] Controversial results have also been published for Si NWs under bending. Zheng et al. reported the large bending strains in Si NWs by a colloidal thin film technique in TEM.[26,32] The Si NWs could be bent to a large strain (21.5%) without cracking. On the contrary, Gordon et al. found that all Si NWs showed linear elastic behavior and brittle failure under bending in AFM.[24]

The controversial results indicate that the mechanical behaviors of Si NWs are complex and depend on the sample geometry/structures, and experimental conditions. The structural variables include the diameter, growth orientation, defects, and so on, and the experimental conditions include the temperature, loading mode, strain rate, and so on. Taking this into account, the structures of samples and experimental conditions in work by Han et al.,[22] by Gordon et al.,[24] and by us are compared (Table 1).

It has been well established that the mechanical behaviors are closely dependent on the structure diameter. Han et al. proposed a mechanism of diameter-related dislocation velocity, $\nu = A\tau^m \exp[-U/(k_BT)]$, where A and m are constants, τ is the shear stress, k_B is the Boltzmann constant, T is the absolute temperature, and U is the activation energy.[22] The activation energy is related to the elastic modulus, which is diameter-dependent. According to their calculations, the activation energy is significantly lower than in the bulk; therefore, small-diameter Si NWs tend to be ductile. The nanowire diameters in Gordon et al.'s work were in the range of 100–700 nm, which are much wider than those in Han et al.'s and our work.

Another difference is the wire orientation. Kang et al. compared the mechanical behaviors of Si NWs with different growth directions.[21,30] It was found that Si NWs with [111] growth directions were more brittle than those with a [110] growth orientation. A ductility parameter was defined to describe the influences of orientations: $A = (S\sigma_C)/(\tau_C)$, where S is the Schmid factor, σ_c is the ideal tensile strength, and τ_c is the ideal shear strength. It was found that the ductility parameter of [110]-oriented Si NWs was larger than that of Si NWs with the [111] growth direction, which means that the former ones are more ductile than the latter ones.[21] In the regarded three works, the Si NWs tested by Han et al. were [110]-oriented, whereas the Si NWs in Gordon et al.'s and our work grew along the [111] direction.

Apparently, the defects should have important influences on the mechanical behaviors of Si NWs. They may act as stress concentrators, nucleation sites for dislocations, and initiation sites for cracks. Surface steps were observed on our samples (Figure S1b). Gordon et al. reported that Si NWs tend to fracture at the twinning planes and sawtooth surface patterns, which may significantly reduce the fracture strength.[24] It was claimed in Han et al.'s publications that their Si NWs were nearly defect-free, which might be one of the reasons for the large plasticity observed.[22,32]

The mechanical properties of Si, especially the brittle-to-ductile (BTD) transition, are sensitive to the strain rate.[53,54] The critical temperature for the BTD transition increased with an increase in the strain rate; the relationship could be described by Arrhenius-type functions. The strain rates in Han et al.'s[22] and our work were around 10^{-5} and 10^{-4}/s, respectively. The loadings were carried out much faster in

Gordon et al.'s work, which used a pushing speed of 10−30 nm/s for the whole cycle distance of 100−300 nm.[24] It was also emphasized that the large plastic strain was obtained at a slow strain rate because the mechanical response depended on the deformation rates.[26]

In addition, as we have demonstrated in the current work, the loading conditions and stress states also have important influences on the mechanical properties of Si NWs, and experimental conditions such as clamping and alignments could affect the outcome.[13−17] Therefore, we emphasize here that the mechanical properties and behaviors of Si NWs are complicated and related to many factors and thus deserve more systematic investigations in the future for a comprehensive understanding.

In conclusion, we found that the mechanical properties and behaviors of Si NWs are closely related to the loading conditions, stress states, and wire diameters by using in situ TEM and MD simulations in tandem. Under uniaxial tension, the Si NWs fractured in a brittle manner by nucleation and propagation of a single crack and cleavage along the (111) planes. As the diameter decreased, the tensile strength tended to increase from 4.4 to 11.3 GPa. Under bending, the Si NWs demonstrated considerable plasticity. In a lower bending strain range (<14%), the Si NWs could be bent repeatedly. At a higher bending strain (>20%), crack nucleation on the tensed side was observed, and on the compressed side, pronounced plastic deformation by dislocation activities and amorphous transition was identified. The present finding of distinct mechanical behaviors of thin Si NWs under different conditions may provide valuable guidance for the design and fabrication of reliable Si-based nanodevices.

ASSOCIATED CONTENT

Ⓢ Supporting Information

Movies of tensile and bending tests by in situ TEM and MD simulations. Detailed description of the MD simulations. TEM images of fractures at different sites. Multiple tensile test results on a single Si NW. This material is available free of charge via the Internet at http://pubs.acs.org.

AUTHOR INFORMATION

Corresponding Author
*E-mail: cliu@imr.ac.cn, golberg.dmitri@nims.go.jp.

Present Address
§Laboratory for Nanophotonics and Electronics, Department of Materials Science and Engineering, Massachusetts Institute of Technology, Cambridge, Massachusetts 02139, United States.

Author Contributions
‖These authors contributed equally to this work.

Notes
The authors declare no competing financial interest.

ACKNOWLEDGMENTS

REFERENCES

(1) Morales, A. M.; Lieber, C. M. *Science* **1998**, *279*, 208−211.
(2) Cui, Y.; Lieber, C. M. *Science* **2001**, *291*, 851−853.
(3) Cui, Y.; Wei, Q. Q.; Park, H. K.; Lieber, C. M. *Science* **2001**, *293*, 1289−1292.
(4) Cui, Y.; Zhong, Z. H.; Wang, D. L.; Wang, W. U.; Lieber, C. M. *Nano Lett.* **2003**, *3*, 149−152.
(5) Feng, X. L.; He, R.; Yang, P.; Roukes, M. L. *Nano Lett.* **2007**, *7*, 1953−1959.
(6) Boukai, A. I.; Bunimovich, Y.; Tahir-Kheli, J.; Yu, J. K.; Goddard, W. A.; Heath, J. R. *Nature* **2008**, *451*, 168−171.
(7) Chan, C. K.; Peng, H. L.; Liu, G.; McIlwrath, K.; Zhang, X. F.; Huggins, R. A.; Cui, Y. *Nat. Nanotechnol.* **2008**, *3*, 31−35.
(8) Wong, E. W.; Sheehan, P. E.; Lieber, C. M. *Science* **1997**, *277*, 1971−1975.
(9) Wu, B.; Heidelberg, A.; Boland, J. J. *Nat. Mater.* **2005**, *4*, 525−529.
(10) Kaplan-Ashiri, I.; Cohen, S. R.; Gartsman, K.; Ivanovskaya, V.; Heine, T.; Seifert, G.; Wiesel, I.; Wagner, H. D.; Tenne, R. *Proc. Natl. Acad. Sci. U.S.A.* **2006**, *103*, 523−528.
(11) Ngo, L. T.; Almécija, D.; Sader, J. E.; Daly, B.; Petkov, N.; Holmes, J. D.; Erts, D.; Boland, J. J. *Nano Lett.* **2006**, *6*, 2964−2968.
(12) Huang, J. Y.; Zheng, H.; Mao, S. X.; Li, Q.; Wang, G. T. *Nano Lett.* **2011**, *11*, 1618−1622.
(13) Zhu, Y.; Espinosa, H. D. *Proc. Natl. Acad. Sci. U.S.A.* **2005**, *102*, 14503−14508.
(14) Agrawal, R.; Peng, B.; Gdoutos, E. E.; Espinosa, H. D. *Nano Lett.* **2008**, *8*, 3668−3674.
(15) Agrawal, R.; Peng, B.; Espinosa, H. D. *Nano Lett.* **2009**, *9*, 4177−4183.
(16) He, M.-R.; Shi, Y.; Zhou, W.; Chen, J. W.; Yan, Y. J.; Zhu, J. *Appl. Phys. Lett.* **2009**, *95*, 091912−091913.
(17) Bernal, R. A.; Agrawal, R.; Peng, B.; Bertness, K. A.; Sanford, N. A.; Davydov, A. V.; Espinosa, H. D. *Nano Lett.* **2010**, *11*, 548−555.
(18) Kizuka, T.; Takatani, Y.; Asaka, K.; Yoshizaki, R. *Phys. Rev. B* **2005**, *72*, 035333.
(19) Tabib-Azar, M.; Nassirou, M.; Wang, R.; Sharma, S.; Kamins, T. I.; Islam, M. S.; Williams, R. S. *Appl. Phys. Lett.* **2005**, *87*, 113102−113103.
(20) Hoffmann, S.; Utke, I.; Moser, B.; Michler, J.; Christiansen, S. H.; Schmidt, V.; Senz, S.; Werner, P.; Gösele, U.; Ballif, C. *Nano Lett.* **2006**, *6*, 622−625.
(21) Kang, K.; Cai, W. *Philos. Mag.* **2007**, *87*, 2169−2189.
(22) Han, X. D.; Zheng, K.; Zhang, Y. F.; Zhang, X. N.; Zhang, Z.; Wang, Z. L. *Adv. Mater.* **2007**, *19*, 2112−2118.
(23) Hsin, C.-L.; Mai, W.; Gu, Y.; Gao, Y.; Huang, C.-T.; Liu, Y.; Chen, L.-J.; Wang, Z.-L. *Adv. Mater.* **2008**, *20*, 3919−3923.
(24) Gordon, M. J.; Baron, T.; Dhalluin, F.; Gentile, P.; Ferret, P. *Nano Lett.* **2009**, *9*, 525−529.
(25) Östlund, F.; Rzepiejewska-Malyska, K.; Leifer, K.; Hale, L. M.; Tang, Y.; Ballarini, R.; Gerberich, W. W.; Michler, J. *Adv. Funct. Mater.* **2009**, *19*, 2439−2444.
(26) Zheng, K.; Han, X.; Wang, L.; Zhang, Y.; Yue, Y.; Qin, Y.; Zhang, X.; Zhang, Z. *Nano Lett.* **2009**, *9*, 2471−2476.
(27) Zhu, Y.; Xu, F.; Qin, Q.; Fung, W. Y.; Lu, W. *Nano Lett.* **2009**, *9*, 3934−3939.
(28) Zhang, D.; Breguet, J.-M.; Clavel, R.; Sivakov, V.; Christiansen, S.; Michler, J. *J. Microelectromech. Syst.* **2010**, *19*, 663−674.
(29) Sohn, Y.-S.; Park, J.; Yoon, G.; Song, J.; Jee, S.-W.; Lee, J.-H.; Na, S.; Kwon, T.; Eom, K. *Nanoscale Res. Lett.* **2010**, *5*, 211−216.
(30) Kang, K. W.; Cai, W. *Int. J. Plast.* **2010**, *26*, 1387−1401.
(31) Steighner, M. S.; Snedeker, L. P.; Boyce, B. L.; Gall, K.; Miller, D. C.; Muhlstein, C. L. *J. Appl. Phys.* **2011**, *109*, 033503−033507.
(32) Wang, L.; Zheng, K.; Zhang, Z.; Han, X. *Nano Lett.* **2011**, *11*, 2382−2385.
(33) Kim, Y.-J.; Son, K.; Choi, I.-C.; Choi, I.-S.; Park, W. I.; Jang, J.-i. *Adv. Funct. Mater.* **2011**, *21*, 279−286.
(34) Meyers, M. A.; Chawla, K. K. *Mechanical Behavior of Materials*; Cambridge University Press: New York, 2009.

(35) Fukata, N.; Sato, K.; Mitome, M.; Bando, Y.; Sekiguchi, T.; Kirkham, M.; Hong, J.-i.; Wang, Z. L.; Snyder, R. L. *ACS Nano* **2010**, *4*, 3807−3816.

(36) Fukata, N. *Adv. Mater.* **2009**, *21*, 2829−2832.

(37) Golberg, D.; Costa, P. M. F. J.; Lourie, O.; Mitome, M.; Bai, X.; Kurashima, K.; Zhi, C.; Tang, C.; Bando, Y. *Nano Lett.* **2007**, *7*, 2146−2151.

(38) Wang, M.-S.; Bando, Y.; Rodriguez-Manzo, J. A.; Banhart, F.; Golberg, D. *ACS Nano* **2009**, *3*, 2632−2638.

(39) Rodriguez-Manzo, J. A.; Wang, M. S.; Banhart, F.; Bando, Y.; Golberg, D. *Adv. Mater.* **2009**, *21*, 4477−4482.

(40) Wang, M. S.; Golberg, D.; Bando, Y. *Adv. Mater.* **2010**, *22*, 93−98.

(41) Wang, M. S.; Golberg, D.; Bando, Y. *Adv. Mater.* **2010**, *22*, 4071−4075.

(42) Wei, X.; Wang, M. S.; Bando, Y.; Golberg, D. *Adv. Mater.* **2010**, *22*, 4895−4899.

(43) Tang, D. M.; Ren, C. L.; Wei, X. L.; Wang, M. S.; Liu, C.; Bando, Y.; Golberg, D. *ACS Nano* **2011**, *5*, 7362−7368.

(44) Golberg, D.; Costa, P. M. F. J.; Wang, M.-S.; Wei, X.; Tang, D.-M.; Xu, Z.; Huang, Y.; Gautam, U. K.; Liu, B.; Zeng, H.; Kawamoto, N.; Zhi, C.; Mitome, M.; Bando, Y. *Adv. Mater.* **2011**, *24*, 177−194.

(45) Wang, M.; Wang, J.; Chen, Q.; Peng, L. M. *Adv. Funct. Mater.* **2005**, *15*, 1825−1831.

(46) Wang, M.; Peng, L. M.; Wang, J.; Chen, Q. *Adv. Funct. Mater.* **2006**, *16*, 1462−1468.

(47) Wang, M.; Kaplan-Ashiri, I.; Wei, X.; Rosentsveig, R.; Wagner, H.; Tenne, R.; Peng, L. *Nano Res.* **2008**, *1*, 22−31.

(48) Courtney, T. H. *Mechanical Behavior of Materials*; McGraw-Hill: Boston, 2000.

(49) Griffith, A. A. *Philos. Trans. R. Soc. London, Sect. A* **1921**, *221*, 163−198.

(50) Hull, R. *Properties of Crystalline Silicon*; INSPEC, The Institution of Electrical Engineers: London, 1999.

(51) Landau, L. D.; Lifshitz, E. M. *Theory of Elasticity*; Pergamon Press: New York, 1986.

(52) Han, X. D.; Zhang, Y. F.; Zheng, K.; Zhang, X. N.; Zhang, Z.; Hao, Y. J.; Guo, X. Y.; Yuan, J.; Wang, Z. L. *Nano Lett.* **2006**, *7*, 452−457.

(53) Samuels, J.; Roberts, S. G.; Hirsch, P. B. *Mater. Sci. Eng., A* **1988**, *105−106*, 39−46.

(54) Brede, M. *Acta Metal. Mater.* **1993**, *41*, 211−228.